Co-seismic deformation and related hazards associated with the 2022 Mw 5.6 Cianjur earthquake in West Java, Indonesia: insights from combined seismological analysis, DInSAR, and geomorphological investigations

Danang Sri Hadmoko, Sandy Budi Wibowo, Dimas Salomo J. Sianipar, Daryono Daryono, Mohammad Naufal Fathoni, Rohanita Setia Pratiwi, Eko Haryono, Franck Lavigne

Geoenvironmental Disasters

RESEARCH

Open Access

Co-seismic deformation and related hazards associated with the 2022 Mw 5.6 Cianjur earthquake in West Java, Indonesia: insights from combined seismological analysis, DInSAR, and geomorphological investigations

Danang Sri Hadmoko[1*], Sandy Budi Wibowo[2], Dimas Salomo J. Sianipar[3], Daryono Daryono[4], Mohammad Naufal Fathoni[1], Rohanita Setia Pratiwi[1], Eko Haryono[1] and Franck Lavigne[5]

Abstract

Introduction On November 21, 2022, a magnitude Mw 5.6 earthquake struck Cianjur Regency in the West Java Province of Indonesia. It was followed by at least 512 aftershocks that persisted from November to June 2023. This seismic event occurred in an area previously unrecognized as an active fault zone. The consequences of this earthquake in Cianjur were severe, leading to both loss of life and extensive structural damage. The substantial damage to buildings was likely a result of abrupt alterations in the local topography due to surface deformation effects.

Objectives This research endeavor aims to spatially determine the patterns of ground surface deformation and its relationship with local geomorphological setting due to earthquakes in Cianjur in 2022.

Methods In this study we conduct seismological analysis of 45 seismic stations, statistical analysis of mainshock and aftershocks data, RADAR Sentinel-1 imagery and employed the DInSAR methodology. Field survey was also conducted to determine the geomorphological characteristics in the study area.

Results The outcomes disclosed that the deformation encompassed both subsidence and uplift. The results signify that there was subsidence deformation in the vicinity of Cianjur and its environs during the primary earthquake on November 21, 2022, with an average deformation value of approximately -5 cm. In contrast, the measured deformation during the aftershocks exhibited uplift deformation, with an average value of 10 cm. The examination of deformation patterns amid the 2022 Cianjur earthquake sequence detects elevated deformation values in the vicinity of Cugenang district, with an orientation running from northwest to southeast. The geomorphological investigation conducted indicates that the region of Cianjur encompasses a variety of landforms, such as volcanic, structural, fluvial, and denudational. These landforms exhibit distinct responses to seismic activities. Co-seismic hazards, such as landslides frequently occur as a consequence of seismic events in mountainous terrain.

Main Conclusions Spatio-temporal variation of ground deformation could arise from various causes, such as the number and distribution of aftershocks, stress redistribution, fault interactions, secondary effects, and local geological settings. The mainshocks release accumulated stress along a fault, resulting in particular types of deformation,

*Correspondence:
Danang Sri Hadmoko
hadmoko@ugm.ac.id
Full list of author information is available at the end of the article

whereas aftershocks may redistribute stress exhibiting on adjacent faults. Secondary effects triggered by aftershocks, coupled with local geological and geomorphological conditions, further contribute to the diverse patterns of ground deformation observed during seismic events. The results of the study revealed that ground deformation had the greatest impact on fluvial, volcanic, and denudational processes, resulting in notable subsidence and uplift in specific regions. The occurrence and magnitude of co-seismic landslides were triggered by both mainshock and aftershock events, which occurred on weathered geological materials. These effects were further amplified by the simultaneous presence of the rainy season.

Implications The knowledge gained from this research can be applied to evaluate the impacts of earthquakes and to proactively reduce future risks.

Keywords Cianjur earthquake, Seismological analysis, Ground deformation, DInSAR and geomorphological investigation, Co-seismic hazard

Introduction

Cianjur is a densely populated regency situated in West Java Province, Indonesia, that faces a heightened risk of earthquakes and associated hazards due to its proximity to several seismically active areas. The Cianjur shallow earthquake (6,84° S–107,05° E) in West Java (Mw 5.6) occurred on November 21, 2022 as shown in Fig. 1. More than 500 aftershocks occurred during first three months after the mainshock that potentially worsened the destruction. Co-seismic ground deformation is the immediate impact associated with the earthquakes that can be triggered by the mainshock and series of aftershocks. It denotes changes on the Earth's surface resulting from the accumulation of tectonic forces within the crust (Wibowo et al. 2021). Ground deformation can therefore be utilized as one of the important parameters to determine the impact of the earthquakes. The scale of ground deformation ranges from mere millimeters to several meters, depending on the earthquake's magnitude and the activity level of the fault (Ozawa et al. 2005; Sato and Une 2016; Yang et al. 2019; Wibowo et al. 2021).

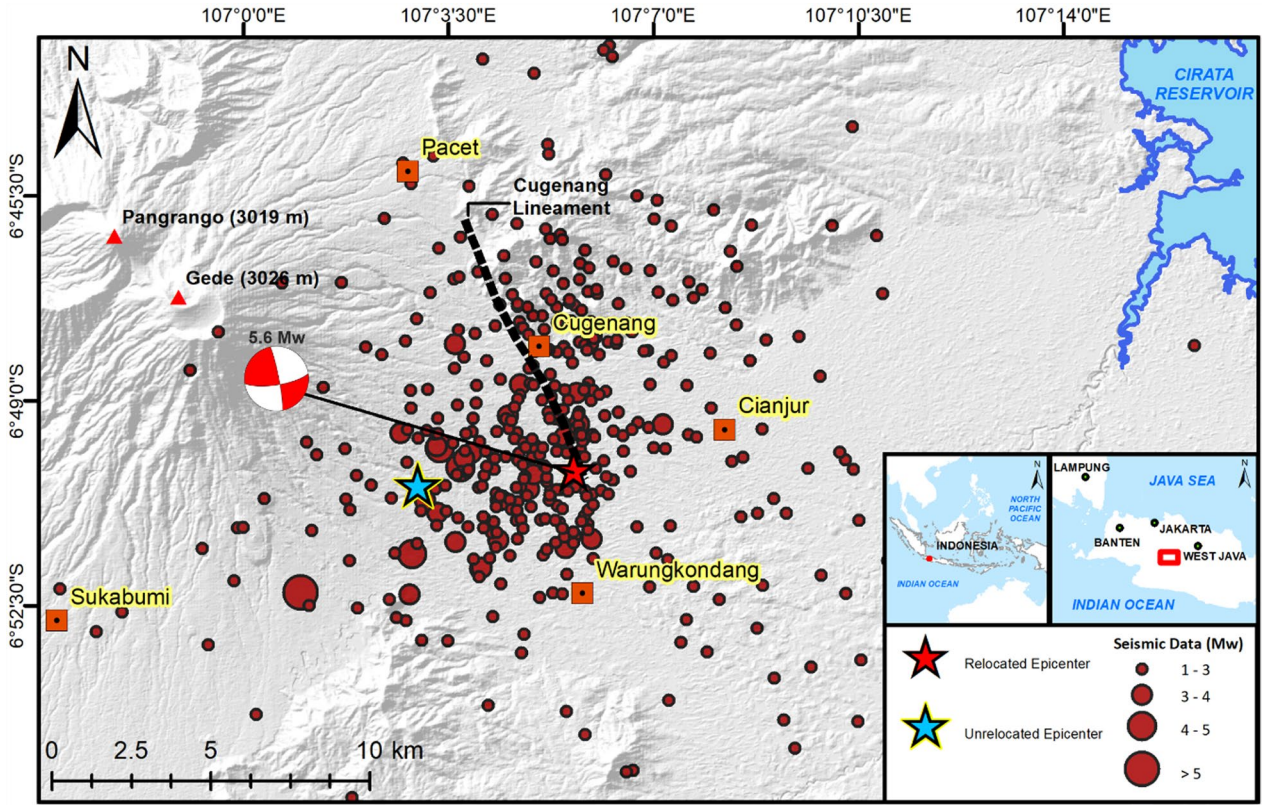

Fig. 1 Study area in Cianjur Regency, Indonesia

Investigating cascading and chain hazards is essential for disaster mitigation efforts. These terms describe the phenomenon where one hazard leads to another, creating a domino effect during catastrophic events (Helbing and Kuhnert 2003; Budimir et al 2014; Zhou et al. 2022). Cascading hazards following the earthquakes have received relatively small attention on disaster risk analysis, since the majority disaster studies have focused on one single hazard (Saputra et al 2021). Under specific geological and geomorphic conditions, one hazard can readily trigger another, with the compounded effects of cascading hazards leading to greater impacts across a broader area than would be anticipated from a single hazard alone (Cutter 2018; Raymond et al. 2020). Cascading hazards initiated by earthquakes are most likely to occur (Goda et al. 2017; Saputra et al. 2021).

Ground deformation, landslides, liquefaction, tsunamis are the most common cascading hazards due to mainshock and aftershocks (Dai et al. 2011; Priya and Pandey 2021; Wibowo et al. 2021; Niraj et al. 2022). The disaster chain-reaction in Palu and Donggala Regency, West Sulawesi Province, was initiated by a 7.4 Mw earthquake on September 28, 2018. Originating from a shallow hypocenter of 10 km, this seismic event led to 554 aftershocks, all registering magnitudes ≥ 3 (Supendi et al 2019). Those earthquakes generated series of complex disasters such as landslides, earthflows, massif ground deformation, tsunamis and caused thousands of fatalities and buildings destruction (Supendi et al. 2019). The southern area of the Palu Basin experienced substantial displacement during the event, with vertical shifts of approximately 5 m and horizontal shifts of around 3 m (Jaya et al 2019). The weakening of surface materials on steep slopes due to earthquakes often leads to co-seismic landslides. These landslides can become more severe with the addition of heavy rainfall throughout the rainy season. A total of ~ 15,700 co-seismic flowslides, rockfalls and debris flows occurred within total area of 43.0 km^2 (Shao et al. 2023).

Visual signs of ground deformation are commonly identifiable directly in the field from the distribution of ground cracks. However, not all the ground deformation can be easily identifiable from the field. Direct field determination of spatial distribution of ground deformation over the larger area is very challenging, therefore, remote sensing approach is needed. Many studies have been conducted to investigate co-seismic ground deformation through remote sensing approach (e.g. Massonnet and Feigl 1995; Feigl et al 1995; Ozawa et al 2005; Bacques et al. 2018; Wibowo et al 2021). Synthetic Aperture Radar Interferometry (InSAR) is a prevalent remote sensing technique utilized to analyze intricate vertical and horizontal ground deformations in the vicinity of the epicenter, offering high spatiotemporal resolution (Wang et al 2021b). The basic principle of InSAR is to determine the interference between two radar images and to measure the displacement both in vertical and horizontal direction (Xinjian et al. 2004). InSAR operates as an active remote sensing technology that emits waves in both vertical and horizontal polarizations towards the Earth's surface, enabling the detection of ground deformations. Wave transmitted from satellite than received back to create radar images. This current contribution is therefore applying InSAR to determine spatio-temporal deformation following the 5.6 Mw Cianjur Earthquake.

This aims of the study are threefold: (a) to analyze the dynamic seismic events using the mainshock and aftershocks data, (b) to determine spatio-temporal distribution of co-seismic ground deformation, (c) to determine the linkage between ground deformation and geomorphological settings. In order to achieve this objective, Sentinel-1 ascending pass Synthetic Aperture Radar (SAR) pictures acquired from around the time of the earthquake up to five months following the event are utilised. This study emphasises the utilisation of post-seismic Interferometric Synthetic Aperture Radar (InSAR) time series for the purpose of ascertaining vertical surface displacement subsequent to the occurrence of an earthquake. In the following parts, we will provide a description of the data and technique employed, as well as a comprehensive analysis and discussion of the obtained results. The primary focus of this study was directed towards examining the relationship between geomorphological characteristics and the proximity of mainshocks to ground deformation.

The study area

Cianjur Regency as the study area of this research holds strategic significance. Cianjur is situated within the West Java Province of Indonesia, a region known for its geological activity and susceptibility to earthquakes. Its close proximity to the epicenter of a significant earthquake that shook the area on November 21, 2022 makes Cianjur particularly compelling for this investigation (Fig. 1). This seismic event was noteworthy in its scale and impact, rendering it a crucial case study for understanding the aftermath of such disasters. The nearness to the earthquake's epicenter means that it experienced the brunt of the seismic forces, resulting in observable ground deformations based on local geomorphological settings. Cianjur regency provides a unique opportunity to examine the immediate consequences of a seismic event on the infrastructure and communities.

The study area exhibits distinctive features of a quaternary volcanic landscape, notably including the Gede-Pangrango volcanic complex in the western region.

These volcanoes are part of the Sunda Arc, a geological region marked by the convergence of the Australian Plate beneath the Eurasian Plate along a tectonic boundary. Gede volcano, classified as dormant, has a documented history of volcanic eruptions. Despite its dormancy, Gede volcano plays a significant role in the geomorphological processes of the area, influencing the development of adjacent land features. As a stratovolcano, it features a prominent elevation and conical structure. The topography of Gede Volcano is characterized by steep and rugged slopes, particularly at higher altitudes, which are laden with volcanic materials, including ash, igneous rocks, and deposits resulting from past lava flows.

Methodology

Seismological analysis

We conducted geophysical investigation by performing seismological methods including analysis of seismic waveform and hypocenter relocation to provide high resolution catalog of Cianjur earthquakes. We utilized the double-difference location algorithm (Waldhauser and Ellsworth 2000) to provide a reliable, more accurate earthquake hypocenter locations. We used seismic data from BMKG, including the picks of the P- and S-waves arrival times at permanent local seismic stations of BMKG (Fig. 4) (e.g., Sianipar et al. 2020). We evaluated the arrival time picks of seismic phase at each station for each detectable event. Employing the double-difference technique relies on the condition that if the separation between the hypocenters of two earthquakes is minor relative to both the distance to the observing station and the scale of velocity heterogeneity, the ray paths to a common station are nearly identical. This similarity allows for the differences in travel times observed at a station to be accurately linked to the spatial displacement between the events.

In the double-difference algorithm, the discrepancies between observed and modeled travel-time differences (double-differences) for two seismic events at a shared station are linked to changes in the relative positions of the hypocenters and their origin times. These adjustments are made possible through the calculation of partial derivatives of the travel times with respect to the unknown variables. The minimization of these double-difference residuals across earthquake pairs at each station is achieved through a weighted least squares approach, utilizing singular value decomposition (SVD) (Waldhauser and Ellsworth 2000). The iterative process involves adjusting the vector differences between adjacent hypocentral pairs and updating the locations and partial derivatives after each iteration. In this study, we used the seismic velocity model extracted from CRUST2.0 model for Cianjur region.

In order to determine the co-seismic deformation occurred during the 2022 Cianjur earthquake, we performed Coulomb stress changes modeling. Based on the Coulomb criterion and focal mechanism theory, the Coulomb stress changes (ΔCFF) can be defined as:

$$\Delta \mathrm{CFF} = \Delta\tau + \mu' \Delta\sigma_{\mathrm{n}} \quad (1)$$

In the context of earthquake dynamics, the Coulomb stress change, represented by Δτ for shear stress changes, μ' as the effective friction coefficient, and Δσn for normal stress changes, quantitatively measures the distribution of aftershocks, alterations in seismicity rates, and the initiation of earthquakes. Typically, areas experiencing higher stress witness a greater number of aftershocks, while regions with reduced stress see a decline in seismicity rates. A change in stress by as little as 0.1 bar is generally considered sufficient to trigger an earthquake (King et al. 1994; Ma et al. 2005; Sianipar et al. 2021). We utilized the Auto Coulomb codes to perform the Coulomb stress changes modeling (Wang et al. 2021a).

DInSAR

In the application of the Two Pass Interferometry technique under the DInSAR framework, two Synthetic Aperture Radar (SAR) images, captured at distinct times, are analyzed in conjunction with a Digital Elevation Model (DEM) to address topographical effects on the phase data (Sacristan 2004). The primary purpose here is to generate an interferogram from these images, which is essential for constructing a subsequent deformation map.

Table 1 List of Sentinel-1 imageries in this research

Mainshocks	Image	Role	Temporal baseline	Aftershocks
21-Nov-22	11-Nov-2022	Master	12 days	166
(Mw 5.6)	23-Nov-2022	Slave		
25-Nov-22	23-Nov-2022	Master	12 days	233
(Mw 4.1)	5-Dec-2022	Slave		
04-Dec-22	5-Dec-2022	Master	12 days	41
(Mw 4.2)	17-Dec-2022	Slave		
–	17-Dec-2022	Master	12 days	41
	29-Dec-2022	Slave		
–	29-Dec-2022	Master	12 days	25
	10-Jan-2023	Slave		
–	10-Jan-2023	Master	12 days	19
	22-Jan-2023	Slave		
–	22-Jan-2023	Master	12 days	8
	3-Feb-2023	Slave		
–	23-Mar-2023	Master	12 days	2
	4-Apr-2023	Slave		

The DEM plays a critical role in mitigating the effects of terrain variations on the interferogram's accuracy. In this research, a set of eight pairs of Sentinel-1 images was employed, and their specific details are outlined in the Table 1.

In the initial stage of RADAR interferometric processing, the first step is referred to as "Top SAR-Split." Its primary objective is to identify a recording burst from the available image data that is well-suited for the study area under consideration. The image modes at our disposal include IW 1, IW 2, and IW 3, with each IW containing 10 bursts. For this process, the chosen polarization type is VV, which is deemed more appropriate for deformation studies due to its emphasis on vertically oriented signal reception. Subsequently, the fundamental step in the generation of interferograms is known as "back-geocoding." This step is designed to align the geometric position of the images and ensure that each pixel, both in terms of range and azimuth, aligns consistently between the master and slave images through the utilization of Enhanced Spectral Diversity (ESD) techniques. Interferogram creation involves processing a pair of SLC data, which consists of both master and slave images, through In-SAR techniques. The primary objective of generating an interferogram is to derive phase and amplitude difference values by computing the phase of the two Sentinel images. Phase computation is the central aspect of interferogram image processing, as it forms the basis for generating interferogram images that exhibit fringe patterns, serving as informative indicators. To enhance the accuracy and precision of the interferometry results, the implementation of multilooking and filtering methods has been adopted. Multilooking, as a process, serves to minimize discrepancies between overlapping subswaths and mitigates noise by averaging multiple observations of the same location. This technique effectively reduces data noise and results in improved image quality. Furthermore, filtering techniques are applied to diminish phase noise in the interferogram, using the Goldstein filtering approach (Goldstein and Wenner., 1998). The integration of these techniques has proven highly effective in generating more dependable and consistent interferometric outcomes.

Furthermore, a topographic correction, often referred to as flattening, is carried out to reduce distortion arising from variations in elevation. This flattening procedure entails computing the disparities in elevation across the observed regions, employing the accessible DEM (Digital Elevation Model) data. The DEM data chosen for this purpose encompass either SRTM 1 Arc-sec or SRTM DEM with a 30-m resolution. The outcome of this procedure is an interferogram displaying a more distinct phase that aligns with the actual elevation characteristics. The data derived from the interferogram processing remains constrained within a range of values spanning from 0 to 2 π, leading to uncertainties in determining the precise ground surface deformation. Consequently, a phase unwrapping procedure becomes imperative to acquire the absolute phase difference. This process involves converting the phase information into metric values by rectifying the transformation using the equation (Ismullah 2004; Rahman et al. 2023):

$$R = \lambda \cdot (\varphi + k) \tag{2}$$

where k denotes the phase ambiguity, a parameter that requires prior determination through the phase unwrapping procedure to derive the absolute phase. n interferometry, the unwrapping of phase data is carried out using the SNAPHU tool, which employs a statistical-cost network-flow algorithm to interpret phase information contained in the interferogram. Following this phase unwrapping, a deformation map is created that visualizes the ground surface movements. These movements are quantified by the Line of Sight (LOS) values, reflecting the displacement along the radar's line of sight. Subsequently, this value undergoes conversion via band mathematics within the SNAP software to derive the vertical displacement value, employing the following formula:

$$\begin{aligned} VD =& (Unwrapping\ phase * 5.5465763) \\ & /(-4 * PI * (cos(rad(inciden\,t\ angle))) \end{aligned} \tag{3}$$

The results obtained from the equation can effectively depict vertical changes in the Earth's surface, manifesting as either uplift or subsidence. To enhance the spatial accuracy of the image and reduce distortions, satellite positioning information is converted into appropriate geographical coordinates. This conversion process is executed through the utilization of Range Doppler terrain correction, facilitated by the SNAP software tool. In this context, the procedure necessitates the availability of a Digital Elevation Model (DEM) as a georeferencing reference. Subsequently, the resultant image undergoes band mathematical calculations to isolate the coherence value, ensuring that the final image possesses a coherence value exceeding 0.2. The selection of this threshold is based on the minimum coherence value requirement stipulated by the European Space Agency (ESA) (European Space Agency, 2023). The DInSAR method is presented in Fig. 2.

Sustained observation through GNSS stations over extended periods is hailed as the optimal benchmark for control measurements (Boni et al. 2018). Nonetheless, this emerged as a constraint in our study due to our inability to execute such comprehensive measurements. This was primarily because Cianjur had not previously encountered significant seismic events, leading

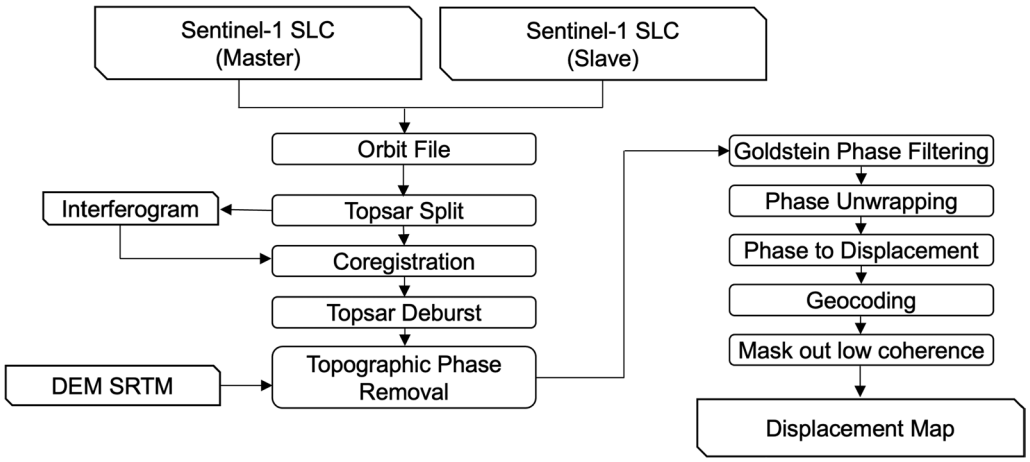

Fig. 2 Flowchart showing the DInSAR Method on spatio-temporal ground deformation assessment

to considerable unpredictability in forecasting epicenter locations. In addition, the immediate aftermath of the earthquake saw the study area become a hive of evacuation efforts owing to structural collapses. This scenario hampered our efforts to deploy GNSS stations post-event. Therefore, the spatial variation of ground deformation was determined at by generating eleven statistical zones, each measuring 1.2 km × 1.2 km, were selected across different geomorphological units. In order to obtain the final deformation result for each selected region, the average deformation values of the pixels inside the training regions were calculated. We conducted an analysis of 8 distinct pairs of ascending images to ascertain the temporal variations in vertical deformation inside the study area between November 11th, 2022 and April 11th, 2023 (Table 1).

Geomorphological mapping

The present investigation utilized geomorphological mapping as a foundational method to ascertain the existence of ground deformation within every geomorphological unit. The landform unit is the geomorphological unit utilized in this study. Landform units are characteristics of the Earth's surface that have a distinctive relief that formed by certain rock types being exposed to geomorphological processes. Geological structures that provide

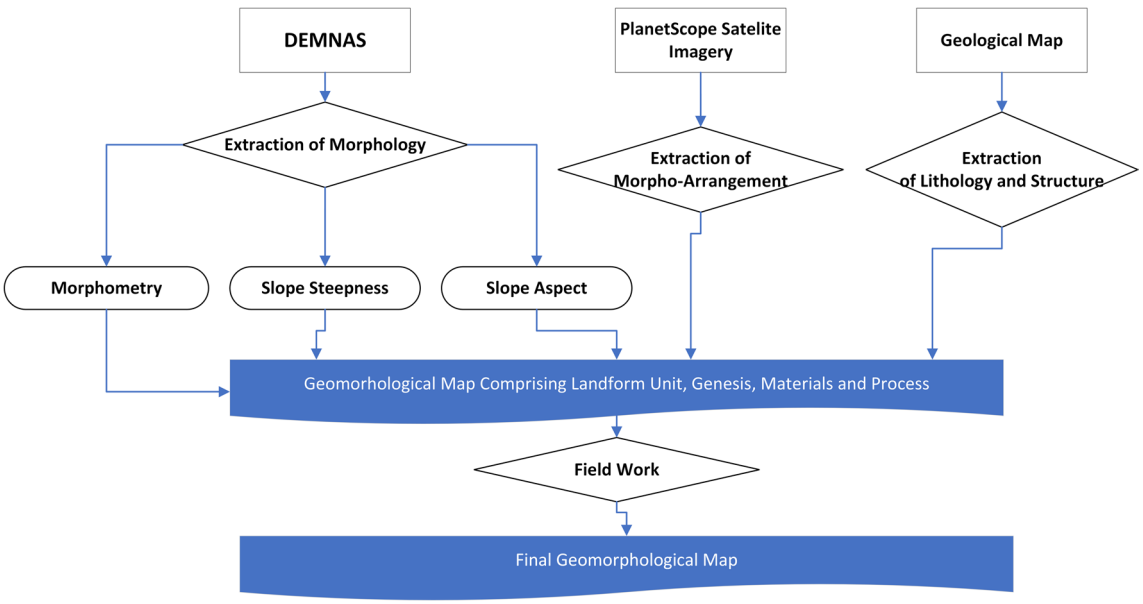

Fig. 3 Flowchart of geomorphological mapping

a variety of responses to earthquake occurrences regulate the geomorphological processes that occur on these materials. The geomorphological mapping is based on morphological characteristics, including morphometry and morphography, morphogenetic aspects that explain how landforms originated, morpho-chronological characteristics, and morpho-association aspects (Fig. 3).

The main spatial data utilized in this study for geomorphological mapping is DEMNAS Data, which is available at https://tanahair.indonesia.go.id/demnas/#/ and was published by the Geospatial Information Agency (BIG) with a spatial resolution of 7.5 m. This information serves as the primary input for creating a landform map that is based on maps of slope steepness, morphology, and morphometry. Data regarding geological features and rock types are taken from the Geological Map, which is created by the Geological Agency of the Republic of Indonesia at a scale of 1: 50,000. Three-meter-resolution PlanetScope® satellite imagery is used to support the landform classification. Using this satellite imagery, the morpho-association data gathering process is finished, and functional maps for fieldwork are created. Fieldwork was done to confirm the interpretation of the geomorphological unit results, pinpoint geomorphological processes, and look for alignment. The geomorphological map serves as a sampling unit for the purpose of computing vertical ground deformation.

Results

Seismic data analysis

The earthquake occurred in November 21th 2022 with magnitude of Mw 5.6 occurred at a depth of 9 km (star symbol in Fig. 4a) was followed by a total of 502 aftershocks (red dots in Fig. 4a) during the period from November 2022 to July 2023. As shown in Fig. 4b, the seismic events recorded varied in depth from 10 km to 122 km, with a concentration of aftershocks primarily occurring within the 10 to 30 km depth range. The temporal variation data of aftershocks indicate that the Cianjur earthquake generated a very high productivity of aftershocks (as seen in Fig. 4b, c), particularly in the first, second, and third months following the main shocks. The frequency of the main shocks in November 2022, December 2022, and January 2023 were recorded as 341, 93, and 47, respectively (illustrated in Fig. 4c). In the subsequent months, up to July 2023, the number of aftershock

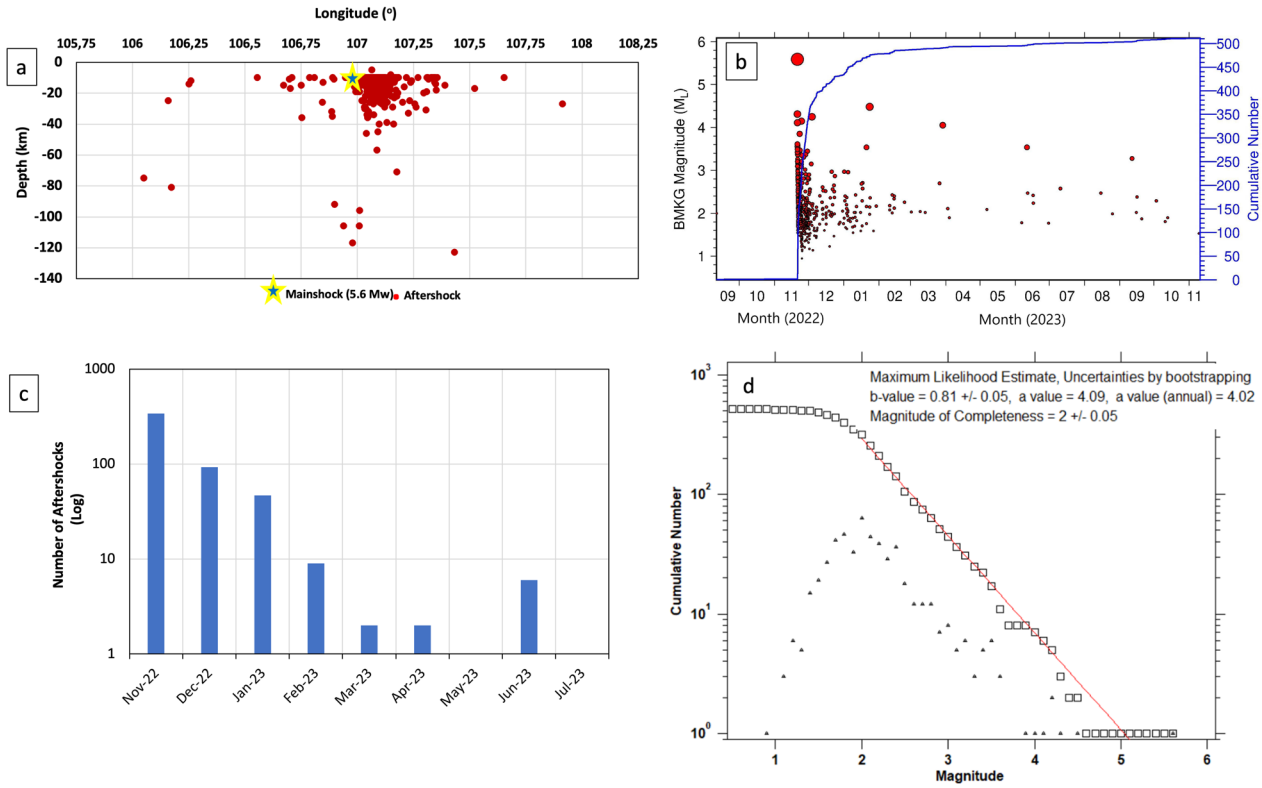

Fig. 4 Mainshocks and aftershocks dynamic in study area from November 2022 to July 2023: **a** distribution of aftershocks on longitude basis versus depth, **b** temporal evolution and cumulative number of the 2022 Cianjur aftershocks, **c** monthly variation of aftershocks presented on logarithmic basis, **d** frequency-magnitude distribution

occurrences per month was less than 10. This trend demonstrates a significant decrease in the frequency of aftershocks. Figure 4b reveals that several of the aftershocks that occurred had magnitudes greater than M 4.0.

The data recorded by 45 seismic stations operated by BMKG demonstrate completeness at a magnitude of M2.0 to accurately identify all earthquakes occurring within the Cianjur aftershocks sequence. The magnitude level signifies the threshold at which there exists a significant likelihood of detecting and recording all seismic events. Furthermore, the temporal decay rate of the aftershocks in Cianjur has an Omori law's p-value of approximately 1.13. The figure might be regarded as an indication of a comparatively rapid decrease in the frequency of aftershocks, implying a swift decline in seismic activity after to the primary seismic event.

The deformation analysis provides a comprehensive understanding of the seismic response to the Cianjur mainshock. The model predicts an average coseismic deformation at depth of approximately 30 cm. Interestingly, no corresponding surface rupture displacement has been detected during the fieldworks, indicating that the deformation may be occurring entirely beneath the surface. Support for this hypothesis comes from the spatial alignment of aftershocks, which are observed to occur along the same fault plane as the mainshock. The aftershocks are spatially associated with areas exhibiting increased Coulomb stress, a result of the coseismic deformation from the Mw 5.6 Cianjur earthquake (highlighted in red in Fig. 5a). The stress calculations were conducted assuming a NNW-SSE orientation of the source fault, computed at a depth of 8 km, and incorporated the fault's specific orientation and slip dynamics with an effective friction coefficient set at 0.4.

Furthermore, if the initial event is considered to have occurred on an E-W trending fault, the subsequent triggering of the north–south trending fault does not align well with the Coulomb stress change predictions (as illustrated in Fig. 5b). This inconsistency suggests that the NNW-SSE trending fault is more likely the causative fault for the Cianjur earthquakes, challenging earlier hypotheses and emphasizing the need for a more nuanced understanding of fault interactions.

Spatio-temporal distribution of co-seismic ground deformation

Figures 6 and 7 display extensive variations in post-seismic LOS displacement, both spatially and temporally. Figure 6a–h depicts the spatial patterns of ground deformation at different time periods. In this study, we employed 8 pairs of distinct images to illustrate the multi-temporal variations in ground deformation occurring during the designated observation timeframe. In addition, To capture the spatio-temporal trends of ground deformation effectively, 11 statistical zones were selected as focal points for monitoring. This approach allowed for an in-depth analysis of multi-temporal patterns between November 11, 2022, and April 4, 2023, with corresponding statistical parameters illustrated in the charts in Fig. 7. The selection of these monitoring area locations is

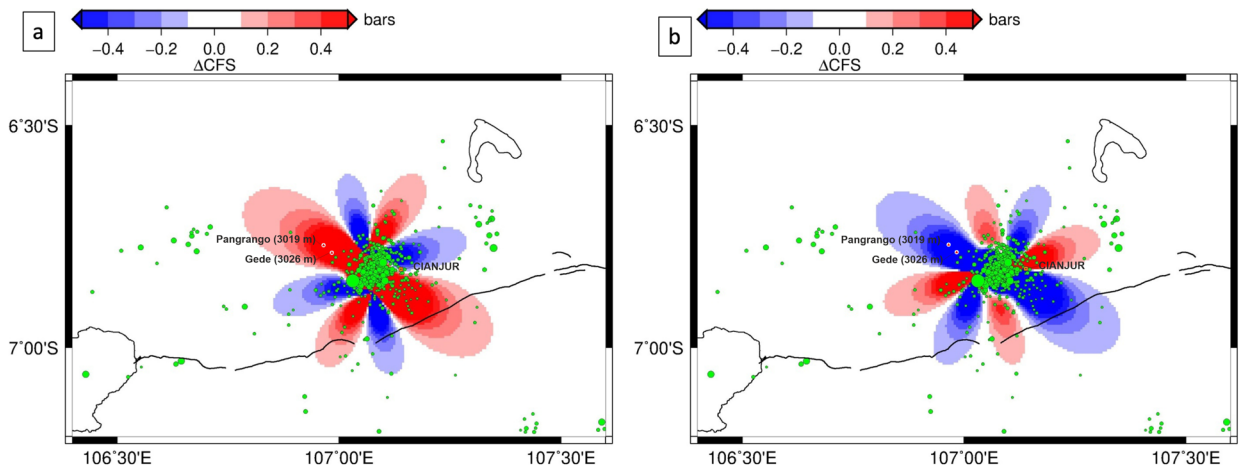

Fig. 5 Calculations of Coulomb stress changes due to the coseismic deformation from the Mw 5.6 Cianjur earthquake were conducted at a depth of 8 km: **a** assuming an NNW-SSE-trending source fault with strike 349°, dip 84°, fault length of about 10 km, average slip of 30 cm, and with an NNW-SSE-trending receiver fault with strike 349°, dip 84°, rake 164°. **b** Assuming an E-W-trending source fault with strike 81°, dip 74°, fault length of about 10 km, average slip of 30 cm, and with an N-S-trending receiver fault with strike 349°, dip 84°, rake 164°. The effective friction coefficient used in both calculations are 0.4

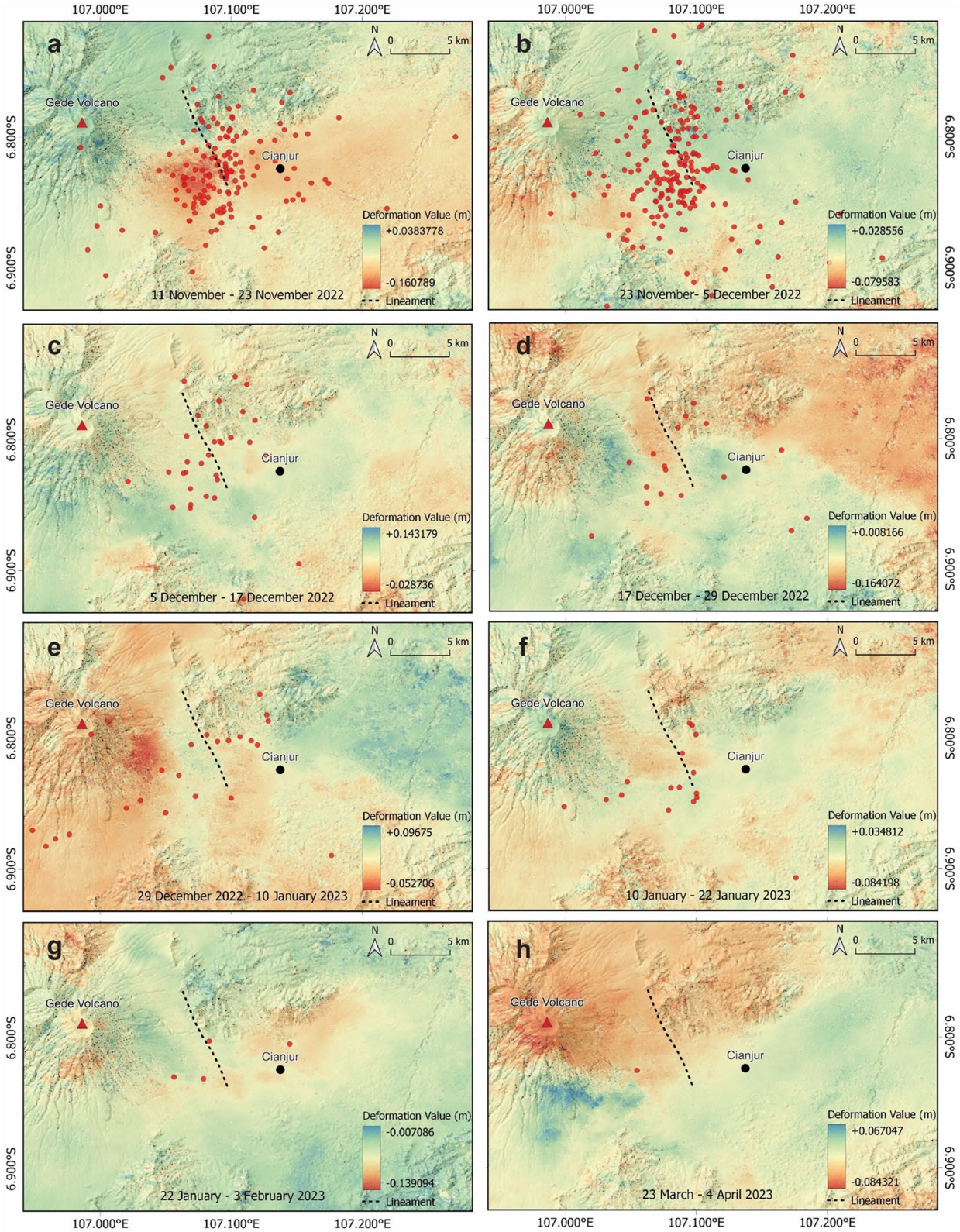

Fig. 6 Spatio-temporal representation of deformation in the study area using DInSAR for the following periods: **a** November 11–23, 2022; **b** November 23–December 5, 2022; **c** December 5–17, 2022; **d** December 17–29, 2022; **e** December 29, 2022–January 10, 2023; **f** January 10–22, 2023; **g** January 22–February 3, 2023; **h** March 23–April 4, 2023. Red dots indicate the locations of aftershocks that occurred during the periods covered by the recorded master and slave images

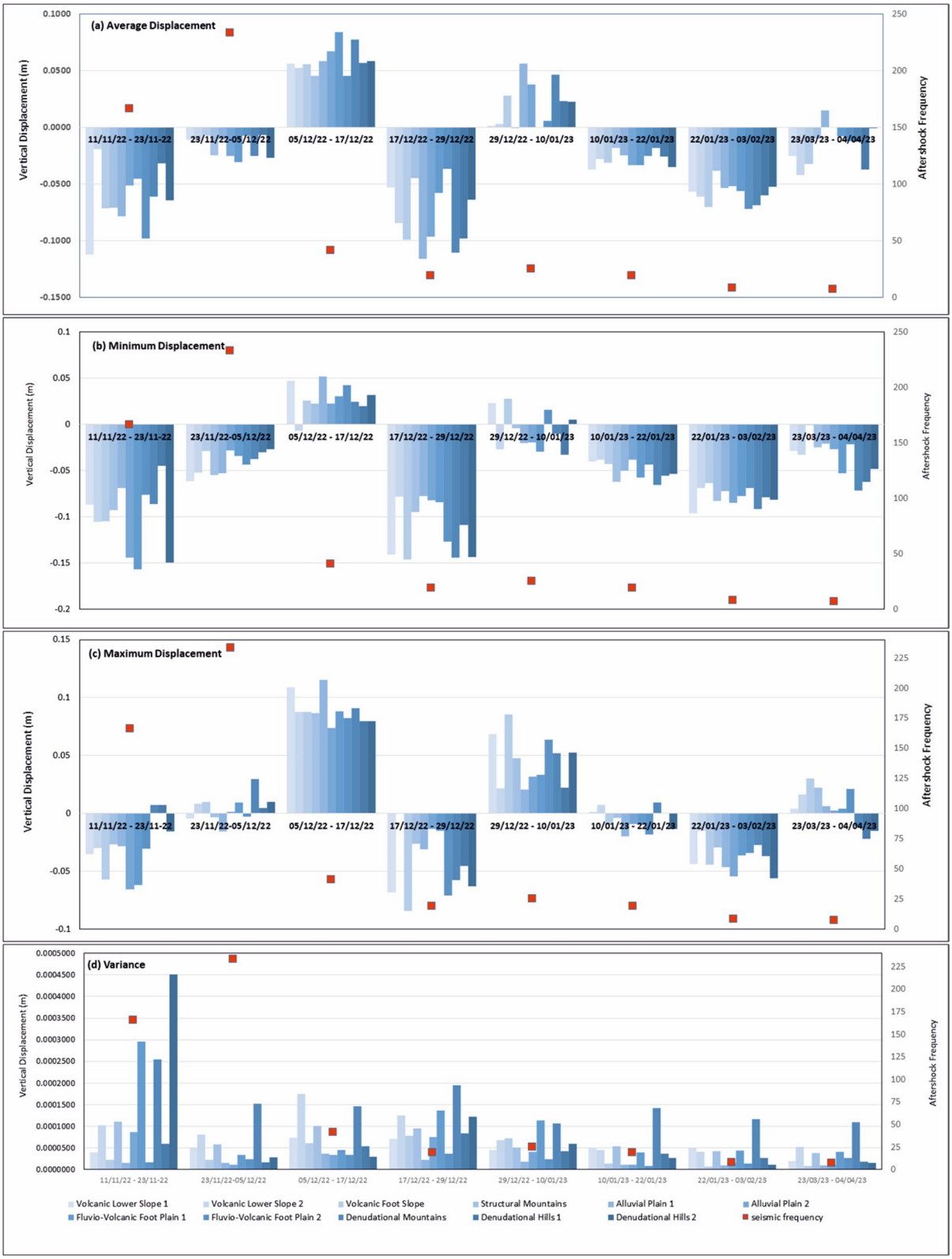

Fig. 7 Spatio-temporal charts showing different statistical parameters of ground deformation on different geomorphological setting: **a** average displacement, **b** minimum displacement, **c** maximum displacement, **d** variance

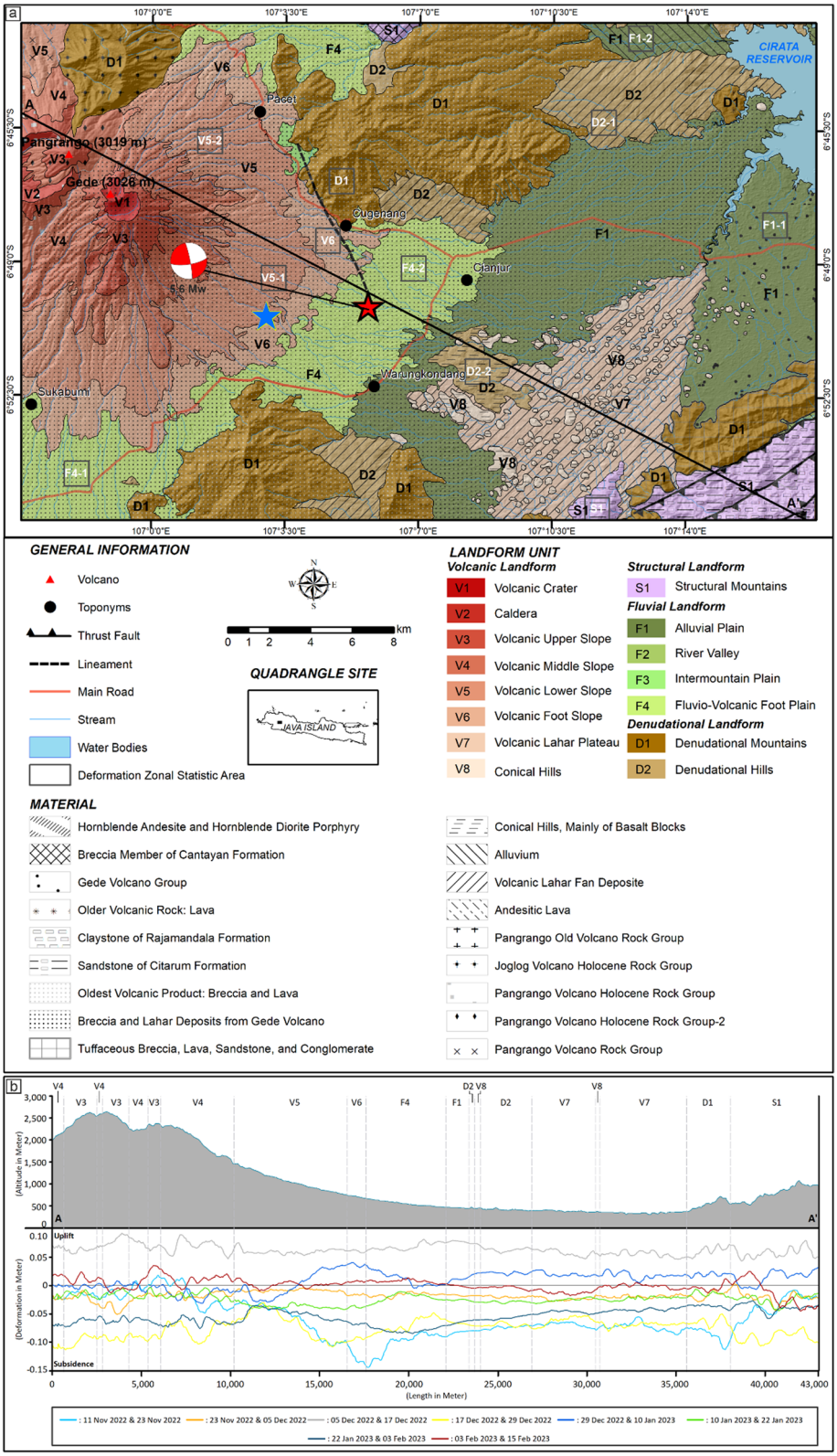

Fig. 8 Geomorphological setting of the study area: **a** geomorphological map showing the information of the landform unit, geological structure and materials and **b** morphological sketch showing relief variation of the cross-section A-B and the spatio-temporal ground deformation following the geomorphological unit

based on variations in landforms, which can be spatially observed in Fig. 8, denoted by red-colored boxes with coded names of the landform.

The vertical displacement values range from − 156 mm (subsidence) to 115 mm (uplifting) in ascending pass for entire area of study area calculated during the period of Nov 11, 2022 to April 11, 2023. In general, the primary characteristic of the deformation data following the seismic event that occurred on November 11, 2022, was subsidence. This phenomena was observed in the majority of the statistical zones over the time periods of November 11th, 2022 to November 23rd, 2022, December 5th, 2022 to December 17th, 2022, December 17th, 2022 to December 29th, 2022, January 10th, 2023 to January 22nd, 2023, January 22nd, 2023 to February 3rd, 2023, and March 23rd, 2023 to April 4th, 2023. Coincidentally, there were instances of uplift observed to a limited degree between the dates of December 5th, 2022, and December 17th, 2022, and predominantly throughout the period from December 29th, 2022, to January 10th, 2023. Regarding the magnitude of land subsidence, a noticeable pattern emerged wherein the subsidence magnitude decreased alongside a decrease in the frequency of aftershocks within the region under investigation.

An abnormality was noted during the initial period following the earthquake, notably from November 11th to November 23rd, and subsequently from December 5th to December 17th, 2022. The documented sequences of aftershocks over these periods were 166 and 233, correspondingly. In contrast to the comparatively higher frequency of aftershocks observed during the period from December 5th to December 17th, the period from November 11th to November 23rd exhibited a notably lower frequency. However, the amount of subsidence was found to be greater during the earlier period. The observed subsidence between November 11th and November 23rd, 2022 can be attributed to the significant impact of the mainshock, which had a magnitude of Mw 5.6. Notwithstanding the notable escalation in aftershock occurrences during the succeeding timeframe, a general decline in the mean subsidence was recorded. Simultaneously, there was a concomitant decrease in the intensity of the aftershocks observed during the specified time period.

In the context of the spatial distribution of land subsidence, maximal average of subsidence were most prominent around the Cugenang and Cianjur subdistricts. These subdistricts not only experienced the mainshock but also had the highest concentration of aftershocks. Moreover, these areas are intersected by a discernible lineament (Fig. 8), running from the Cugenang Subdistrict in a NNW to SSE orientation. In addition to these subdistricts, relatively substantial average land subsidence occurred across the plains within the central zone of the study area. This was particularly noticeable in the period from November 11th, 2022, to November 23rd, 2022, when the mainshocks were recorded. Such subsidence is reflected in zonal statistics Fluvio-Volcanic Plain (F4-2) (− 98 mm), Volcanic Lower Slope (V5-1) (− 110 mm), and Volcanic Foot Slope (V6) (− 71 mm), all located in the plain areas. Contrastingly, zonal statistic 9, in proximity to the mainshock, shows a significantly lesser degree of ground deformation (− 30 mm), and the minimal land subsidence was recorded in zonal statistic Denudational Mountain (D1) (− 19 mm), both of which are situated in mountainous regions.

Spatio-temporal data analysis of DInSAR (Fig. 6a–h) has elucidated substantial variations in terms of the distribution of areas undergoing either uplifting or subsidence. A notably stark contrast was observed in the period from December 17th, 2022 to December 29th, 2022 (Fig. 6d), during which a significant subsidence was recorded in the north-eastern section of the study area—a spatial phenomenon not mirrored in data from other recording dates. Additionally, the recordings from March 23rd to April 4th, 2023 (Fig. 6h), indicated significant subsidence in the north-western region, a distinctive occurrence not noted in the other datasets.

Geomorphology and ground deformation

The research area has complex geomorphological characteristics, consisting of volcanic processes, structural processes in the form of uplifts, denudational processes dominated by weathering, erosion, and landslides of old volcanic materials, and fluvial processes dominated by volcanic deposits carried by lahar flows and river currents (Fig. 8). Volcanic landforms are dominant in the study area, constituting approximately 34.47% of the total coverage. These landforms are primarily concentrated in the western and central regions. Notable examples include Volcanic Craters (V1), Calderas (V2), Volcanic Upper Slope (V3), Volcanic Middle Slope (V4), Volcanic Lower Slope (V5), Volcanic Foot Slope (V6), Volcanic Lahar Plateau (V7), and Conical Hills (V8). Volcanic deposits encompass a variety of lithologies, lava flow, including breccia, tuffaceous sandstone, and shale, which are widely distributed across the volcanic terrain and originated from Gede and Pangrango Volcanoes. The deposition of lahars, which exhibit a lack of sorting and consist of andesitic boulders, gravels, and sands, occurs on V4, V5, V6, and V7.

Structural landforms are found on the south-eastern part, namely Structural Mountainous (S), that cover a small part of the study area. This structural landform was constructed through an uplifting process during the Miocene and Oligocene. This landform is spitted by two

perpendicular thrust faults stretching in the direction of south-west and north-east and making a very distinct scarp and nearly vertical slope along the Faultline. The materials are dominated by claystone, sandstone, and breccia.

The central part of the study area features fluvial landforms that make up 33.49% of its total coverage. Those landforms are Alluvial Plain (F1), River Valley (F2), Intermountain Basin (F3), and Fluvio-Volcanic Foot Plain (F4). Those fluvial landforms are well developed due to the excessive sedimentation following the Gede and Pangrango Volcanic Complex eruptions during the quaternary period, which are characterized by the presence of very thick alluvium deposits (3 m), laharic deposits, Breccia-Andesite, and tuffaceous sandstone. On the slopes of Gede Volcano, there is a strong likelihood that lahars, which are essentially volcanic mudflows or debris flows, have occurred previously. These lahars can flow down the steep slopes during or after volcanic eruptions, carrying volcanic debris, rocks, and sediment. Lahar deposits may be visible on the lower slopes and in valleys, serving as evidence of past volcanic activity. The region surrounding Gede Volcano is dissected by river valleys. These valleys serve as drainage channels for rainwater and runoff from the mountain's slopes. River valleys can be deeply incised by lahars, thus containing sediment transported from the volcano and surrounding areas.

In the northeastern region of Cianjur lies the Cirata Reservoir. Lacustrine deposits within the Cirata Reservoir have formed through the sedimentation of materials at the bottom of the reservoir over time. The primary contributor to these deposits is the Citarum River, which discharges into the reservoir, transporting a diverse array of sediments including silt, clay, and organic matter. The fine-grained texture of these sediments, particularly silt and clay, is attributed to the tranquil environment within the reservoir. Over time, these sediments settle at the bottom, forming cohesive layers. Additionally, organic materials such as plant debris and microorganisms are preserved within these deposits. Denudational Landform consists of Denudational Mountains (D1) spread at the northern and southern part covering 28.5% of the study area. Denudational Mountains is characterized by the deep valley on V shapes dissected the entire area of the mountains. Weathering, erosion, and mass movement process of volcanic deposits are obviously visible on the landform. The materials were formed during the period of Pliocene.

To evaluate the role of geomorphology in ground deformation, a comparison of ground deformation at eleven statistical zone points across different geomorphological units was performed. The deformation data presented in the graph of Fig. 7 indicates that during the initial period of the earthquake, the average of vertical deformation from November 11, 2022, to November 23, 2022, the three geomorphological units experiencing the greatest subsidence were the Volcanic Lower Slope (V5-1), Fluvio-Volcanic Plain 2 (F4-2), and Alluvial Plain 1 (F4-1) with subsidence amounts of − 112.50 mm, − 98.25 mm, and − 78.37 mm respectively. In the period from November 23, 2022, to December 5, 2022, the units with the largest subsidence were Fluvio-Volcanic Foot Plain 1 (F4-1), Denudational Hills 1 (D2-1), and Alluvial Plain 2 (F1-2) with respective values of − 30.96 mm, − 26.82 mm, and − 25.56 mm. For the period from December 17, 2022, to December 29, 2022, the units with the greatest subsidence were Alluvial Plain 1 (F1-1), Denudational Hill 1 (D2-1), and Denudational Mountain (D1) with values of − 11.63 mm, − 11.05 mm, and − 9.81 mm respectively. During the period from January 22 to February 3, 2023, the geomorphological units with the most significant subsidence were Volcanic Foot Slope (V1), Fluvio-Volcanic Foot Plain 2 (F4-2), and Denudational Hills 1 (D2-1) with values of − 11.63 mm, − 11.05 mm, and − 9.81 mm respectively. According to this data, most cases of the three highest subsidence rankings are almost always related to fluvial processes, volcanic processes, and denudational processes.

Regarding the uplift that occurred from December 5, 2022, to December 17, 2022, the geomorphological units that experienced the most significant uplift were the Fluvio-Volcanic Foot Plain (F4-1), Denudational Hill 1 (D2-1), and Alluvial Plain 2 (F1-1), with values of 83.69 mm, 77.33 mm, and 66.97 mm respectively. Meanwhile, in the period from December 29, 2022, to January 10, 2023, the greatest uplift occurred in Alluvial Plain 1, Denudational Hill 1, and Alluvial Plain 2 with magnitudes of 55.96 mm, 46.30 mm, and 37.79 mm respectively. This indicates a similar finding that the greatest uplift is also associated with landforms originating from fluvial and denudational processes.

The cross-section AA' (shown in Fig. 8b) displays the spatiotemporal evolution of post-seismic deformation and its correspondence with the topographical sequence. This plot details the temporal development of ground deformation across different cross-sectional landforms, highlighting the interplay between ground deformation and geomorphological characteristics. We observed the steepest curve occurred during the period of mainshock in the vicinity of the epicenter and Cugeneng Faultline, indicating the most significant ground deformation after the main earthquakes, crossing three landform units V5, V6 and F4.

Fig. 9 Field evidence of ground failure due to an earthquake in Cugenang District, Cianjur Regency, West Java: **a** uplifting and subsidence visible from a dirt road and cracking in a dike, **b** cracks in the asphalt road indicating soil deformation, **c** liquefaction resulting in the collapse of buildings (photos taken by Pratiwi)

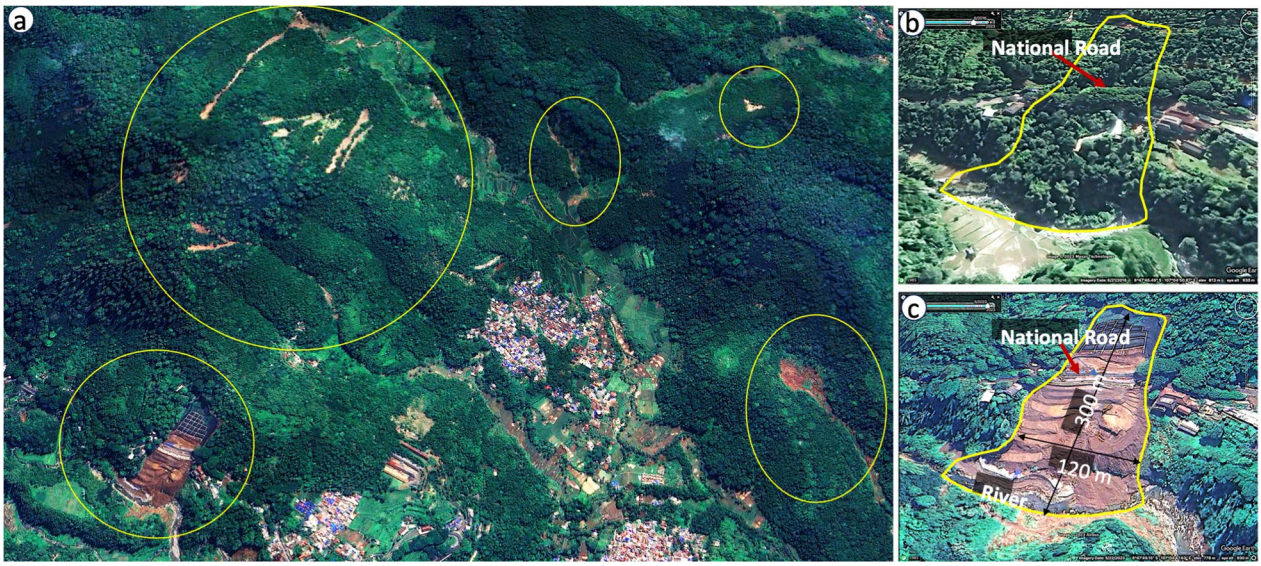

Fig. 10 Aerial Images captured from Google Earth showing the distribution of landslide at the northern part of the study area: **a** distribution of major landslides, **b** slope view before landslide in Cugenang and **c** slope view after the landslide occurred that claimed dozens of losses of life in Cugengang

Variance analysis has been conducted across various statistical zones to understand fluctuations or variations in the data distribution of maximum uplifting and maximum subsidence relative to the average value. These parameters indicate the presence of areas that are most unstable and undergo significant vertical changes. The largest fluctuations are consistently shown by the denudational hills landforms (D2), which over time tend to

have the highest variance, indicating that these landforms experience the greatest fluctuations in uplifting and subsidence. From the data, it can be noted that there is generally a gradual decrease in variance values over time, coinciding with a decrease in aftershock activity.

Several evidences of ground failure were readily apparent in the fields, evidenced by cracks appearing in the soil, along asphalt roads, and beside road dikes, as depicted in Fig. 9a, b. These photographs explicitly document ground deformations, including uplifting and subsidence. Furthermore, in the Cugenang region, liquefaction occurred within thick alluvial deposits, leading to the tilting of concrete structures to the left, as highlighted in Fig. 9c. This field evidence definitively confirms the occurrence of morphological changes in the study area due to the earthquake. However, the considerable thickness of the sediment layers obscured any visual identification of fault features during field inspections, indicating a need for more detailed geophysical and geological studies.

Co-seismic landslides

Over 50 major landslides of various sizes occurred following the earthquake in Cianjur (Fig. 10a). A major landslide, measuring 300 m in length, 120 m in width, and 25 m in depth, occurred approximately 6 km northeast of the earthquake's epicentre (Fig. 10b, c). Fig. 10b and c demonstrate the significant changes in the slope prior to and following a landslide. This landslide is a combination of a rotational landslide process that transformed into an earthflow. Most of these landslides took place in denudational mountainous terrains characterized by steep and rugged topography with slope inclinations exceeding 30°. The region's lithology, dominated by volcanic deposits from Mount Gede, aligns with the landslide direction due to the southeastward flow of sediments during deposition. This alignment, combined with the presence of unstable layers like breccia, lahar, and impermeable tuff, heightened the risk of landslides. Observations from the landslide locations reveal that most occurred in forested areas with dense vegetation cover. This indicates that despite good land cover, the external factor of an earthquake serves as a significant trigger for landslides.

The landslides were triggered by seismic activities during the rainy season, despite the area's previous stability. Additionally, human activities, such as improper slope cuttings for road construction and land use changes from forests to plantations, have destabilized the slopes. This is particularly evident in Cugenang, with landslides reaching depths of 8–12 m exemplifying the impact of both geological and anthropogenic factors in the region.

Discussion

We performed an extensive examination of the 2022 Mw 5.6 Cianjur earthquake through the integration of various seismological methodologies: statistical analysis, spatiotemporal analysis, a high-resolution earthquake catalogue, and a coulomb stress variations model. The statistical analysis yielded significant findings regarding the frequency, distribution, and magnitude of seismic occurrences in the area. This enabled us to situate the Cianjur earthquake in the larger context of seismic activity in the region. In contrast, the spatiotemporal analysis provided a comprehensive perspective of the earthquake's temporal and spatial evolution. The identification of a north–south (NNW-SSE) orientation as the most probable fault causing the Cianjur earthquake aligns with previous research findings, as suggested by Supendi et al. (2023a, b). In addition, the mainshock induced an increase in stress towards the NNW and WSW directions. This observation is based on their analysis of Coulomb stress changes, which correlates with the spatial distribution of aftershocks in these areas (Supendi et al. 2023a, b).

However, the findings of our field investigations indicate a significant lack of surface rupture. In general, surface ruptures serve as indicators of fault lines, presenting evident proof of their boundaries and orientations (Sianipar et al. 2021). Their presence frequently contributes substantially to the comprehension of earthquake mechanics. The absence of surface ruptures during the Cianjur earthquake implies that a more intricate network of subsurface fault mechanisms may have been at work. The lack of surface ruptures suggests the necessity for more extensive geophysical investigations. In order to achieve a comprehensive understanding of the fault dynamics that contributed to the Cianjur earthquake, further comprehensive and meticulous geophysical investigations are necessary. Conducting such investigations is critical for deciphering the intricacies of the subsurface fault system and will yield a more comprehensive assessment of the seismic hazards at study area.

Considering the range of deformation values derived from the eight maps (Figs. 6 and 7), there is a notable variability in these measurements. With respect to the earthquake's epicenter locations, regions consistently showing signs of subsidence deformation, particularly with higher values in the image pair taken between November 11 and November 23, as well as between December 17 and December 29, are situated to the north of the epicenter. These results exhibit a consistent pattern, oriented in a northwest direction, extending towards Cugenang and the Pacet Sub-district. In essence, these subsidence-prone areas are part of the broader Cianjur basin on Fluvio-Volcanic Foot Plain (F4) and Alluvial Plain.

Furthermore, the image pair captured between November 19 and December 1 reveals an intriguing pattern in this area, characterized by a significant uplift variation of up to 12 cm around Cugenang. This pattern also follows the same northwest-southeast orientation.

The analysis of deformation images reveals a noticeable trend: as one moves closer to the Warungkondang and Cianjur Sub-districts, there is a decrease in deformation values. However, it is worth noting that this trend is reversed in the image pair captured between December 1 and December 13, which is contrary to initial expectations. In general, these findings align with the hypothesis that deformation values, encompassing both subsidence and uplift, tend to diminish as the distance from the earthquake epicenter increases (Wibowo et al. 2021; Al Shawa et al. 2021; Vaka et al. 2023). Nevertheless, the eight image pairs obtained in the southern slope region and the vicinity of Mt. Gede Pangrango exhibit inconsistencies in the deformation results. The deformation values consistently surpass the overall mean in these areas. Furthermore, both the Mt. Gede Pangrango region and the northeastern portion of the study area's slope tend to display relatively substantial disparities in deformation values. In particular, the image pairs acquired between December 1 and December 13 and between December 17 and December 29, the Mt. Gede Pangrango area presents intricate deformation patterns that encompass both subsidence and uplift, which is similar to other earthquake series striking a small volcanic island, Lombok in 2018 (Wibowo et al. 2021). Each event does not produce similar vertical direction of deformations, but there is alternance between uplift and subsidence for each event especially for mainshocks containing different magnitudes and epicenter next to the volcanic cone.

Furthermore, within the eight sets of image pairs (Fig. 8), the northeastern hillside area, particularly on Denudational Hills presents a convoluted pattern of deformation. Notably, there are substantial discrepancies in deformation values even in proximate areas. Despite the considerable distance of Mt. Gede and the hillside regions from the earthquake epicenter, the resulting deformation values, comprising both uplift and subsidence, are surprisingly elevated. Furthermore, the nature of these deformations varies considerably, suggesting the involvement of intricate geological processes (Shan et al. 2004, Huang et al. 2019; Dong et al. 2020; Prajapati and Mishra 2021). The elevated values mentioned earlier can be attributed to processing errors stemming from image quality. In terms of topography, these notably high deformation values consistently manifest in regions characterized by hilly or mountainous terrain. In certain instances, DInSAR processing may encounter difficulties in accurately gauging deformations in areas with intricate topographical variations. Such regions, marked by complex topography, can introduce significant disparities in elevation, leading to geometric effects and fluctuations in the viewing angles of complex RADAR reflection signals. High variation of topography can lead to phase unwrapping errors and reduced coherence. These issues complicate the process of obtaining accurate deformation measurements (e.g. Darwish et al. 2021; Thomas 2021; Bhattarai et al. 2017). Consequently, this affects the consistency of DInSAR results. In addition to these topographical factors, it has been previously noted that the influence of the variation of the coherence and interferogram image quality can introduce very sensitive in variation of deformation. Throughout the phase unwrapping stage, the intricate nature of the terrain introduces its own set of difficulties, as the unwrapping process becomes notably more intricate when compared to relatively flat regions. Unwrapping errors present a significant processing hurdle in DInSAR, given that they have the potential to undermine the quality of deformation outcomes.

Vegetation covers also play a crucial role in affecting DInSAR's performance. Dense vegetation areas are known to cause lower coherence in DInSAR signals, which in turn reduces the accuracy of the measurements. However, employing specific techniques and wavelengths, such as L-band radar, has been shown to mitigate these effects and provide more reliable results in heavily vegetated regions (e.g. Andersen et al. 2005). Furthermore, atmospheric conditions, particularly variations in water vapor, introduce additional errors into DInSAR measurements (Serkhane et al. (2022). Addressing these atmospheric delays through the use of models or supplementary data sources is critical for enhancing the accuracy of DInSAR across diverse topographic settings (Remy et al. 2003). Another important factor influencing DInSAR's performance is vegetation covers. Lower coherence in DInSAR signals is known to result from dense vegetation areas, which lowers measurement accuracy. In densely vegetated areas, however, it has been demonstrated that using particular methods and wavelengths—like L-band radar—mitigates these effects and yields more accurate results (e.g. Andersen et al. 2005). Moreover, atmospheric factors introduce additional errors into DInSAR measurements, especially variations in water vapour. Improving the accuracy of DInSAR in a variety of topographic settings requires addressing these atmospheric delays with models or additional data sources (Hanssen 2001; Remy et al. 2003).

To ascertain the consistency of the deformation results acquired through DInSAR processing, the processed deformation maps, represented in the eight image pairs, were cross-referenced with earthquake distribution

data provided by the BMKG. The examination of these deformation maps alongside the spatial distribution of earthquake epicenters during the Cianjur earthquake sequence from November to December reveals a notable correspondence. The regions exhibiting pronounced deformation in the maps align with the central epicenter area of the earthquake sequence. The seismic data collected for this period illustrate a distribution pattern of epicenters predominantly clustered around the vicinity of Cugenang. This alignment corresponds with the findings of the DInSAR processing, consistently demonstrating significant deformation values near Cugenang. Consequently, a correlation is established between the deformation pattern derived from DInSAR processing and the spatial distribution of earthquake epicenters. These facts suggest that the ground deformation that occurred is likely not only controlled by the distance to the mainshock, but also by the frequency of aftershocks in the surrounding region of the observation point and the geomorphological attributes of the area, such as landform units representing surface materials, ongoing geomorphological processes, and morphology.

Regarding the differential interferograms generated, it is critical to highlight the spatial coherence within the displacement field. Field observations have led to the inference that the rupture was subterranean, as it remained invisible on the Earth's surface. Field survey did not show any evidence of the seismic fault. The concept is supported by the spatial distribution of secondary geodynamic occurrences, such as cracks, rockfalls, and landslides, over the mountainous region of the northern part of the study area. The fact is also similar to what happened in Athens related to the earthquake in 1999 as proposed by Foumelis et al. (2009).

The spatial distribution of the largest magnitude land deformation occurred in the area of Volcanic Foot Slope of the Young Pangrango Volcano and in the Alluvial Plain near Cugeneng and Cianjur. This is indicated by the sharp descending slope of the curve of DInSAR on November 11–23, 2022 in Fig. 7b. Several factors could be determining that this area has the largest ground deformation i.e.: (1) the region is dominated by thick young alluvial deposits from the Quaternary period which cause a significant Peak Ground Acceleration value of about 0.5 g for the Mw 5.6 earthquake (Supendi et al. 2022, 2023a, b), (2) the area is close to the Cugeneng fault that splits towards NNW and SSE and is adjacent to the earthquake's epicentre, (3) the area is an urbanized area with relatively high population density and a very significant level of building damage. Fluvial landscapes, such as the alluvial plains, are characterized by loosely packed, water-saturated sediments that are susceptible to liquefaction during seismic activity. Due to this phenomenon, soil particles become dispersed and become liquid-like, which causes ground deformation and subsidence. Similar to this, when shaken, heterogeneous volcanic ash and deposits found in volcanic lower slopes and fluvio-volcanic plains can settle or slump, leading to subsidence. Denudational Hills and other denuded areas are also vulnerable to destabilization during seismic events, which can result in landslides and slumping, which can cause subsidence through material displacement and resettlement. Therefore, in the context of earthquake mitigation, building codes become very important to achieve earthquake-resistant buildings. This analysis not only sheds light on the Cianjur earthquake sequence but also provides a crucial insight into the seismic hazard assessment and potential for future seismicity in the region (e.g Irsyam et al. 2020), driving home the importance of robust seismic monitoring and targeted geophysical investigations.

Co-seismic landslides as part of hazard chains are frequently observed following seismic events, particularly in regions characterized by mountainous terrain. The seismic activity resulting from the earthquake induces the movement of substantial amounts of weathered material, leading to the initiation of landslide motion. The spatial distribution of ground deformation and observed co-seismic landslides were similar, i.e. along the Cianjur Fault and aggravated by the presence of La Nina during the period of earthquakes. Similar incidents were seen in other locations in Indonesia, such as the seismic event that occured on Lombok Island, West Nusa Tenggara in 2018 (Zhao et al. 2021), as well as the Palu earthquake that occurred in the same year (Zhao 2021). The occurrence of the co-seismic landslides in Cianjur was further intensified by the concurrent rainy season period observed in November. Further research is crucially needed to mitigate the presence of hazard chains caused by earthquakes, especially in wet tropical areas. Special attention must be given, especially when an earthquake occurs in mountainous and hilly areas, particularly during the rainy season. Co-seismic landslides are very likely to occur as a result of the chain impact caused by already unstable soil due to an earthquake, exacerbated by soil saturation due to high rainfall. Often, these co-seismic landslides will trigger further chain hazards in the form of debris flow when the soil becomes saturated due to high rainfall (Zhou et al. 2022).

Due to the moderate spatial resolution of Sentinel-1, data presents limitations for detailed local or site-specific observations. At that scale, accuracy will be significantly determined by conditions of land cover change, topography, atmospheric conditions, and the nature of the land surface. In this case of spatial accuracy, utilizing GNSS data from different locations would improve the accuracy of ground deformation monitoring. However,

since the objective of this current contribution is to to determine spatio-temporal distribution of co-seismic ground deformation in large area and due to the unavailability of GNSS data, we applied DInSAR analysis to complement the limitation. DInSAR deformation measurements in different part of the world resulted reasonable accuracy e.g. of 6 mm (Dong et al. 2021), less than 8 mm (Duan et al. 2020) or even 5 mm (Manuta et al. 2019; Wang et al. 2010). Since its launch in 2014, the open data policy and ongoing global surveillance facilitated by Sentinel-1 SAR data have markedly improved the ability to perform measurements and monitoring of ground deformation on a global scale. This enhancement in accuracy and resolution has been achieved through the application of InSAR time series analysis, as noted by Ganas et al. (2018); Morishita et al. (2023).

The current contribution has a wide range of potential applications. It can improve structural resilience particularly infrastructure development and urban planning by pointing out locations vulnerable to co-seismic landslides or deformation, allowing for better-informed planning. More geophysical research is necessary, as evidenced by the intricate network of subsurface fault mechanisms and the lack of surface ruptures. The thorough analysis demonstrates the multifaceted approach needed to comprehend and reduce seismic hazards, making it suitable for use as a case study in geoscience education. In addition, the study can direct efforts to mitigate geological and environmental hazards, such as managing the risk of landslides and promoting conservation. Insurance companies can more accurately assess risk and customize insurance products for properties in earthquake-prone areas by using the detailed deformation patterns and hazard chains that have been identified. The research can be used by policymakers to create or improve regulations pertaining to building codes, community resilience initiatives, and disaster risk reduction.

Conclusion

This comprehensive study focuses on the utilization of a high-resolution seismic approach derived from 45 seismic stations operated by BMKG to accurately identify and characterize an earthquake that occurred in Cianjur Regency, West Java Province, Indonesia. The employment of seismic techniques at a high resolution has proven to be important in locating and understanding this disastrous seismic event. Furthermore, the study extends its analysis to encompass the spatio-temporal distribution of co-seismic ground deformation in the study area. By harnessing the capabilities of Sentinel 1 satellite imageries, the research captures the dynamic changes in vertical deformation resulting from the seismic activity. The use of Radar satellite imageries adds a crucial dimension to the study, allowing for a comprehensive examination of the extent and evolution of ground deformation over both space and time. The significance of this research lies in its integrative approach, bringing together three key methodologies: ground deformation analysis, high-resolution seismic investigation, and a geomorphological survey. Through the combination of these diverse techniques, the study achieves the whole understanding of the interplay between ground deformation patterns and the underlying geomorphological settings of the studied area. The findings hold implications for understanding earthquake dynamics, assessing associated risks, and informing strategies for mitigating the impact of such events in regions with similar geomorphological characteristics.

Acknowledgements
We acknowledge the invaluable contributions of the anonymous reviewers and the editor whose feedback has substantially improved this manuscript. Appreciation is also extended to the Directorate of Research at Universitas Gadjah Mada for their financial support, the Laboratory of Environmental Geomorphology and Disaster Mitigation, Faculty of Geography, Universitas Gadjah Mada, and colleagues at the Meteorological, Climatological, and Geophysical Agency of Indonesia (BMKG) for their engaging discussions and provision of seismic data. We are grateful to the European Space Agency and the Geospatial Agency of Indonesia for supplying Sentinel imagery and DEMNAS data, and to IRD France for funding travel to the Bandung workshop under the SIR Project.

Author contributions
Conceptualization: DSH, SBW; seismological analysis: DSJS, DD; DInSAR Analysis: SBW, DSH, RSP, Geomorphological Mapping: DSH, MNF, Fieldworks: DSH, SBW, MNF, RSP, writing original draft preparation: DSH, SBW, writing, review and editing: DSH, SBW, DSJS, DD, FL, EH, Figure editing: MNF, RSP, DSH, funding acquisition, DSH, FL. Authors have read and agreed to the published version of the manuscript.

Funding
The research was financially supported by the Program Peningkatan Academic Excellence 2023 from Universitas Gadjah Mada, Yogyakarta, as specified in Order Letter No. 7725/UN1.P.II/Dit-Lit/PT/01.03/2023.

Availability of data and materials
All data are presented in this article.

Declarations

Competing interests
The authors declare that they have no competing interests regarding the publication of this paper.

Author details
[1]Laboratory of Environmental Geomorphology and Disaster Mitigation, Faculty of Geography, Universitas Gadjah Mada, Sekip-Bulaksumur, Yogyakarta, Indonesia. [2]Laboratory of Geographic Information Science, Faculty of Geography, Universitas Gadjah Mada, Sekip-Bulaksumur, Yogyakarta, Indonesia. [3]State College of Meteorology, Climatology, and Geophysics (STMKG), Tangerang Selatan, Indonesia. [4]Agency for Meteorology, Climatology, and Geophysics of the Republic of Indonesia (BMKG), Jakarta, Indonesia. [5]Laboratoire de Geographie Physique, Univerité Paris 1 Panthéon Sorbonne, Paris, France.

Received: 25 November 2023 Accepted: 19 April 2024
Published online: 07 May 2024

References

Al Shawa O, Atzori S, Doglioni C, Liberatore D, Sorrentino L, Tertulliani A (2021) Coseismic vertical ground deformations vs intensity measures: examples from the Apennines. Eng Geol 293:106323. https://doi.org/10.1016/j.enggeo.2021.106323

Andersen H, Reutebuch S, McGaughey R (2005) Accuracy of an IFSAR-derived digital terrain model under a conifer forest canopy. Can J Remote Sens 31:283–288. https://doi.org/10.5589/m05-016

Bacques G, de Michele M, Foumelis M et al (2020) Sentinel optical and SAR data highlights multi-segment faulting during the 2018 Palu-Sulawesi earthquake (Mw 7.5). Sci Rep 10:9103. https://doi.org/10.1038/s41598-020-66032-7

Bhattarai R, Alifu H, Maitiniyazi A, Kondoh A (2017) Detection of land subsidence in Kathmandu Valley, Nepal, using DInSAR technique. Land 6:39. https://doi.org/10.3390/land6020039

Bonì R, Bosino A, Meisina C, Novellino A, Bateson L, McCormack H (2018) A methodology to detect and characterize uplift phenomena in urban areas using sentinel-1 data. Remote Sens 10:607. https://doi.org/10.3390/rs10040607

Budimir MEA, Atkinson PM, Lewis HG (2014) Earthquake-and-landslide events are associated with more fatalities than earthquakes alone. Nat Hazards 72:895–914. https://doi.org/10.1007/s11069-014-1044-4

Cutter SL (2018) Linkages between vulnerability and resilience, Chapter 12. In: Fuchs S, Thaler T (eds) Vulnerability and resilience to natural hazards. Cambridge University Press, Cambridge, pp 257–270

Dai FC, Xu C, Yao X, Xu L, Tu XB, Gong QM (2011) Spatial distribution of landslides triggered by the 2008 Ms 8.0 Wenchuan earthquake, China. J Asian Earth Sci 40(4):883–895. https://doi.org/10.1016/j.jseaes.2010.04.010

Darwish N, Kaiser M, Koch M, Gaber A (2021) Assessing the accuracy of ALOS/PALSAR-2 and sentinel-1 radar images in estimating the land subsidence of coastal areas: a case study in Alexandria City, Egypt. Remote Sens 13:1838. https://doi.org/10.3390/rs13091838

Dong Y, Meng G, Hong S (2020) Coseismic and postseismic deformation of the 2016 Mw 6.6 Aketao earthquake from InSAR observations and modelling. Pure Appl Geophys 177:265–283. https://doi.org/10.1007/s00024-019-02092-9

Dong J, Lai S, Wang N, Wang Y, Zhang L, Liao M (2021) Multi-scale deformation monitoring with Sentinel-1 InSAR analyses along the Middle Route of the South-North Water Diversion Project in China. Int J Appl Earth Obs Geoinf 100:102324. https://doi.org/10.1016/j.jag.2021.102324

Duan W, Zhang H, Wang C, Tang Y (2020) Multi-temporal InSAR parallel processing for Sentinel-1 large-scale surface deformation mapping. Remote Sens 12:3749. https://doi.org/10.3390/rs12223749

European Space Agency (2023) InSAR principles: guidelines for SAR interferometry processing and interpretation. Accessed: Aug. 01, 2023. https://www.esa.int/esapub/tm/tm19/TM-19_ptA.pdf.

Feigl KL, Sergent A, Jacq D (1995) Estimation of an earthquake focal mechanism from a satellite radar interferogram: application to the December 4, 1992 Landers aftershock. Geophys Res Lett 22(9):1037–1040. https://doi.org/10.1029/94GL03212

Foumelis M, Parcharidis Is, Lagios E, Voulgaris N (2009) Evolution of post-seismic ground deformation of the Athens 1999 earthquake observed by SAR interferometry. J Appl Geophys 69(1):16–23. https://doi.org/10.1016/j.jappgeo.2009.02.007

Ganas A, Kourkouli P, Briole P, Moshou A, Elias P, Parcharidis I (2018) Coseismic displacements from moderate-size earthquakes mapped by sentinel-1 differential interferometry: the case of February 2017 Gulpinar earthquake sequence (Biga Peninsula, Turkey). Remote Sens 10(7):1089. https://doi.org/10.3390/rs10071089

Goda K, Petrone C, De Risi R, Rossetto T (2017) Stochastic coupled simulation of strong motion and tsunami for the 2011 Tohoku, Japan earthquake. Stoch Environ Res Risk Assess 31:2337–2355. https://doi.org/10.1007/s00477-016-1352-1

Goldstein RM, Werner CL (1998) Radar interferogram filtering for geophysical applications. Geophys Res Lett 25(21):4035–4038. https://doi.org/10.1029/1998GL900033

Hanssen RF (2001) Radar interferometry: data interpretation and error analysis, vol 2. Kluwer Academic Publishers, Dordrecht. https://doi.org/10.1007/0-306-47633-9

Helbing D, Kuhnert C (2003) Assessing interaction networks with applications to catastrophe dynamics and disaster management. Physica A 328(3–4):584–606. https://doi.org/10.1016/S0378-4371(03)00519-3

Huang Z, Zhang G, Shan X, Gong W, Zhang Y, Li Y (2019) Co-seismic deformation and fault slip model of the 2017 Mw 7.3 Darbandikhan, Iran-Iraq earthquake inferred from D-InSAR measurements. Remote Sens. https://doi.org/10.3390/rs11212521

Indonesian Geospatial Agency (BIG) Digital Elevation Model and National Bathymetric Data (DEMNAS) link: https://tanahair.indonesia.go.id/demnas/#/

Irsyam M, Cummins PR, Asrurifak M, Faizal L, Natawidjaja DH, Widiyantoro S, Meilano I, Triyoso W, Rudiyanto A, Hidayati S, Ridwan M (2020) Development of the 2017 national seismic hazard maps of Indonesia. Earthq Spectra 36(1_suppl):112–136. https://doi.org/10.1177/8755293020951206

Ismullah IH (2004) Pengolahan Fasa untuk Mendapatkan Model Tinggi Permukaan Dijital (DEM) pada Radar Apertur Sintetik Interferometri (INSAR) Data Satelit. Prosiding ITB Sains & Tek 36A(1):11–32 (**(In Indonesian Languange)**)

Jaya A, Nishikawa O, Jumadil S (2019) Distribution and morphology of the surface ruptures of the 2018 Donggala-Palu earthquake, Central Sulawesi, Indonesia. Earth Planets Space 71:144. https://doi.org/10.1186/s40623-019-1126-3

King GC, Stein RS, Lin J (1994) Static stress changes and the triggering of earthquakes. Bull Seismol Soc Am 84(3):935–953. https://doi.org/10.1785/BSSA0840030935

Ma KF, Chan CH, Stein RS (2005) Response of seismicity to Coulomb stress triggers and shadows of the 1999 Mw= 7.6 Chi-Chi, Taiwan, earthquake. J Geophys Res Solid Earth. https://doi.org/10.1029/2004JB003389

Manunta M, De Luca C, Zinno I, Casu F, Manzo M, Bonano M, Fusco A, Pepe A, Onorato G, Berardino P et al (2019) The Parallel SBAS approach for Sentinel-1 Interferometric Wide swath deformation time-series generation: algorithm description and products quality assessment. IEEE Trans Geosci Remote Sens 57:6259–6281. https://doi.org/10.1109/TGRS.2019.2904912

Massonnet D, Feigl KL (1995) Satellite radar interferometric map of the co-seismic deformation field of the M = 6.1 Eureka Valley, California Earthquake of May 17, 1993. Geophys Res Lett 22(12):1541–1544. https://doi.org/10.1029/95GL01088

Morishita Y, Sugimoto R, Nakamura R, Tsutsumi C, Natsuaki R, Shimada M (2023) Nationwide urban ground deformation in Japan for 15 years detected by ALOS and Sentinel-1. Prog Earth Planet Sci 10:66. https://doi.org/10.1186/s40645-023-00597-5

Niraj KC, Gupta SK, Shukla DP (2022) Kotrupi landslide deformation study in non-urban area using DInSAR and MTInSAR techniques on Sentinel-1 SAR data. Adv Space Res 70(12):3878–3891. https://doi.org/10.1016/j.asr.2021.11.042

Ozawa T, Nishimura S, Wada Y, Ohkura H (2005) Coseismic deformation of the Mid Niigata prefecture Earthquake in 2004 detected by RADARSAT/InSAR. Earth Planet Space 57:423–428. https://doi.org/10.1186/BF03351828

Prajapati SK, Mishra OP (2021) Co-seismic deformation and slip distribution of 5 April 2017 Mashhad, Iran earthquake using InSAR sentinel-1A image: implication to source characterization and future seismogenesis. Nat Hazards 105:3039–3057. https://doi.org/10.1007/s11069-020-04440-8

Priya T, Pandey AC (2021) Geoinformatics-based assessment of land deformation and damage zonation for Gorkha earthquake, 2015, using SAR interferometry and ANN approach. SN Appl Sci 3:573. https://doi.org/10.1007/s42452-021-04574-9

Rahman AAA, Majid NA, Ahli NA, Latip ASA, Taib AM (2023) The capability of SNAP software application to identify landslide using InSAR technique. Phys Chem Earth Parts a/b/c. https://doi.org/10.1016/j.pce.2023.103427

Raymond C, Horton RM, Zscheischler J, Martius O, AghaKouchak A, Balch J, Bowen SG, Camargo SJ, Hess J, Kornhuber K, Oppenheimer M, Ruane AC, Wahl T, White K (2020) Understanding and managing connected extreme events. Nat Clim Change. https://doi.org/10.1038/s41558-020-0790-4

Remy D, Bonvalot S, Briole P, Murakami M (2003) Accurate measurements of tropospheric effects in volcanic areas from SAR interferometry data: application to Sakurajima volcano (Japan). Earth Planet Sci Lett 213:299–310. https://doi.org/10.1016/S0012-821X(03)00331-5

Sacristan O (2004) Advanced differential interferometric SAR techniques for detection terrain and building displacement. Dissertation, Universitat Politechnica De Catalunya

Saputra A, Gomez C, Delikostidis I, Zawar-Reza P, Hadmoko DS, Sartohadi J (2021) Preliminary identification of earthquake triggered multi-hazard and risk in Pleret Sub-District (Yogyakarta, Indonesia). Geo-Spat Inf Sci 24(2):256–278. https://doi.org/10.1080/10095020.2020.1801335

Sato HP, Une H (2016) Detection of the 2015 Gorkha earthquake-induced landslide surface deformation in Kathmandu using InSAR images from PALSAR-2 data. Earth Planets Space 68:47. https://doi.org/10.1186/s40623-016-0425-1

Serkhane A, Benfedda A, Guettouche MS, Bouhadad Y (2022) InSAR derived co-seismic deformation triggered by the Mihoub (Tell Atlas of Algeria) 28 May 2016 (Mw = 5.4) earthquake combined to geomorphic features analysis to identify the causative active fault. J Afr Earth Sci 188:104476. https://doi.org/10.1016/j.jafrearsci.2022.104476

Shan X, Ma J, Wang C, Liu J, Song X, Zhang G (2004) Co-seismic ground deformation and source parameters of Mani M79 earthquake inferred from spaceborne D-InSAR observation data. Sci China Ser D Earth Sci 47:481–488. https://doi.org/10.1360/01yd0424

Shao Z, Wu Y, Ji L, Diao F, Shi F, Li Y, Long F, Zhang H, Wang W, Wei W, Wang P, Liu X, Liu Q, Pan Z, Yin X, Liu Y, Feng W, Zou Z, Cheng J, Lu R, Xu Y, Li X (2023) Assessment of strong earthquake risk in the Chinese mainland from 2021 to 2030. Earthq Res Adv. https://doi.org/10.1016/j.eqrea.2022.100177

Sianipar D, Sipayung R, Ulfiana E (2020) Excessive seismicity over a limited source: the August 2019 earthquake swarm near Mt. Salak in West Java (Indonesia). J Seismol 24:1189–1204. https://doi.org/10.1007/s10950-020-09957-w

Sianipar D, Daniarsyad G, Priyobudi P, Heryandoko N, Daryono D (2021) Rupture behavior of the 2017 MW6.6 Poso earthquake in Sulawesi, Indonesia. Geod Geodyn 12(5):329–335. https://doi.org/10.1016/j.geog.2021.07.002

Supendi P, Nugraha AD, Widiyantoro S, Abdullah CI, Puspito NT, Palgunadi KH, Daryono D, Wiyono SH (2019) Hypocenter relocation of the aftershocks of the Mw 7.5 Palu earthquake (September 28, 2018) and swarm earthquakes of Mamasa, Sulawesi, Indonesia, using the BMKG network data. Geosci Lett 255:112298. https://doi.org/10.1186/s40562-019-0148-9

Supendi P, Winder T, Rawlinson N, Bacon CA, Palgunadi KH, Simanjuntak A, Kurniawan A, Widiyantoro S, Nugraha AD, Shiddiqi HA, Ardianto D, Adi SP, Karnawati D, Priyobudi, MarliyaniImranJatnika GIIJ (2023a) A conjugate fault revealed by the destructive Mw 5.6 (November 21, 2022) Cianjur earthquake, West Java, Indonesia. J Asian Earth Sci 257:105830. https://doi.org/10.1016/j.jseaes.2023.105830

Supendi P, Priyobudi, Jatnika J, Sianipar D, Ali YH, Heryandoko N, Daryono Prayitno Adi S, Karnawati D, Anugerah SD, Fatchurochman I, Sudrajat A (2023) Analisis Gempabumi Cianjur (Jawa Barat) Mw 5.6 Tanggal 21 November 2022. https://inatews.bmkg.go.id/ (In Indonesian Language)

Thomas A (2021) Mapping of surface deformation associated with the 5.2 magnitude Stilfontein earthquake of 3 April 2017 using radar interferometry. Egypt. J. Remote Sens. Space Sci. 24(1):85–108. https://doi.org/10.1016/j.ejrs.2020.01.005

Vaka DS, Rao YS, Bhattacharya A (2023) Time series analysis of the pre-seismic and post-seismic surface deformation of the 2017 Iran-Iraq earthquake derived from Sentinel-1 InSAR data. J Earth Syst Sci 132:64. https://doi.org/10.1007/s12040-023-02085-2

Waldhauser F, Ellsworth WL (2000) A double-difference earthquake location algorithm: method and application to the northern Hayward fault, California. Bull Seismol Soc Am 90(6):1353–1368

Wang Z, Liu G, Chen T, Zhang J, Huang G (2010) Detecting and assessing the land subsidence in coal mining area using PALSAR data based on D-InSAR technique. In: ICCET 2010—2010 international conference on computer engineering technology proceedings, vol 3, pp 222–226

Wang J, Han P, Li G (2021a) The extraction and analysis of deformation features of Hualien earthquake based on Sentinel-1A/B SAR data. J Indian Soc Remote Sens 49:2069–2077. https://doi.org/10.1007/s12524-021-01377-8

Wang J, Xu C, Freymueller JT, Wen Y, Xiao Z (2021b) AutoCoulomb: an automated configurable program to calculate Coulomb stress changes on receiver faults with any orientation and its application to the 2020 M W 7.8 Simeonof Island, Alaska, earthquake. Seismol Soc Am 92(4):2591–2609

Wibowo SB, Hadmoko DS, Isnaeni Y, Farda NM, Putri AFS, Nurani IW, Supangkat SH (2021) Spatio-temporal distribution of ground deformation due to 2018 Lombok earthquake series. Remote Sens 13(11):2222. https://doi.org/10.3390/rs13112222

Yang G, Lu Z, Zhang Q, Liu R, Ji L, Zhao C (2019) Ground deformation and fissure activity in Datong basin, China 2007–2010 revealed by multi-track InSAR. Geomatics, Natural Hazards and Risk, pp 465–482. https://doi.org/10.1080/19475705.2018.1529711

Zhao B (2021) Landslides triggered by the 2018 Mw 7.5 Palu supershear earthquake in Indonesia. Eng Geol 294:106406. https://doi.org/10.1016/j.enggeo.2021.106406

Zhao B, Liao H, Su L (2021) Landslides triggered by the 2018 Lombok earthquake sequence, Indonesia. CATENA 207:105676. https://doi.org/10.1016/j.catena.2021.105676

Zhou W, Qiu H, Wang L, Pei Y, Tang B, Ma S, Yang D, Cao M (2022) Combining rainfall-induced shallow landslides and subsequent debris flows for hazard chain prediction. CATENA 213:106199. https://doi.org/10.1016/j.catena.2022.106199

Publisher's Note